APPLIED OPTICS

10.1126/sciadv.1600027

Self-rolling and light-trapping in flexible quantum well–embedded nanomembranes for wide-angle infrared photodetectors

Han Wang,[1,2] Honglou Zhen,[1] Shilong Li,[1] Youliang Jing,[1,2] Gaoshan Huang,[3] Yongfeng Mei,[3]* Wei Lu[1]*

Three-dimensional (3D) design and manufacturing enable flexible nanomembranes to deliver unique properties and applications in flexible electronics, photovoltaics, and photonics. We demonstrate that a quantum well (QW)–embedded nanomembrane in a rolled-up geometry facilitates a 3D QW infrared photodetector (QWIP) device with enhanced responsivity and detectivity. Circular geometry of nanomembrane rolls provides the light coupling route; thus, there are no external light coupling structures, which are normally necessary for QWIPs. This 3D QWIP device under tube-based light-trapping mode presents broadband enhancement of coupling efficiency and omnidirectional detection under a wide incident angle (±70°), offering a unique solution to high-performance focal plane array. The winding number of these rolled-up QWIPs provides well-tunable blackbody photocurrents and responsivity. 3D self-assembly of functional nanomembranes offers a new path for high conversion efficiency between light and electricity in photodetectors, solar cells, and light-emitting diodes.

INTRODUCTION

Self-assembly of inorganic nanomembranes (*1*, *2*) offers great opportunities to build up micro- and nanoscale devices in three-dimensional (3D) geometry (*3*, *4*). A flat nanomembrane can be mechanically wrinkled, rolled, twisted, and stretched (*4*) for various applications, such as stretchable electronics (*5*), micro- and nanorobotics (*6*), bioinspired microsystems (*7*), 3D photonics (*8*, *9*), and flexible and wearable sensor systems (*10*–*12*). Bioinspired digital cameras (*7*) and spherical solar cells (*13*, *14*) are typical examples of using 3D designs in optoelectronic and photovoltaic applications. Photodetectors, especially infrared detectors, which provide another application in optoelectronics, are widely used in daily life and for research studies. Quantum well (QW) infrared photodetectors (QWIPs), which are third-generation infrared detectors, have attracted much attention (*15*, *16*) because of the advantages of matured material growth technique and good content uniformity over a large area (*17*). However, the low quantum efficiency of QWIPs due to the intrinsic intersubband transition (ISBT), as compared with that of direct bandgap transition infrared detectors (for example, HgCdTe photodetectors), results in a relatively low responsivity and detectivity. In addition, only the incident light with an electric field parallel to the QW stacking direction can be absorbed by QWIPs, according to the so-called polarization selection rule (*15*, *17*). Therefore, various optical grating and arrayed coupling designs have been developed to enhance the light absorption efficiency of QWIP devices (*18*–*24*).

Here, we demonstrate that QW-embedded nanomembranes without a light coupling design can self–roll up and form 3D infrared photodetectors with enhanced responsivity and detectivity. These self–rolled-up photodetectors present omnidirectional detection under a wide incident angle of ±70°. Broadband enhancement of coupling efficiency is observed in this tube-based light-trapping system. Rolled-up QWIPs with various winds exhibit well-tunable photocurrents and responsivity. 3D assembly and architecture enable nanomembranes to function with high conversion efficiency between light and electricity, which could suggest other applications in some devices, such as solar cells and light-emitting diodes, and can be adapted to different detection mechanisms and various material systems for enhanced photodetection.

[1]National Laboratory for Infrared Physics, Shanghai Institute of Technical Physics, Chinese Academy of Sciences, 500 Yutian Road, Shanghai 200083, China. [2]University of Chinese Academy of Sciences, 19 Yuquan Road, Beijing 100049, China. [3]Department of Materials Science, Fudan University, 220 Handan Road, Shanghai 200433, China.
*Corresponding author. Email: yfm@fudan.edu.cn (Y.M.); luwei@mail.sitp.ac.cn (W.L.)

RESULTS AND DISCUSSION

3D tubular QWIPs were produced from 2D planar QWIP nanomembranes on the basis of rolled-up nanotechnology. The planar QWIP nanomembrane was made of single crystalline III to V semiconductors and grown by metal-organic chemical vapor deposition (MOCVD). It is composed of a GaAs substrate, an AlAs sacrificial layer, an InAlGaAs strained layer, a GaAs bottom contact layer, a thin AlAs corrosion block layer, a GaAs/AlGaAs QW functional layer, a GaAs conductive layer, another AlAs corrosion block layer, and a GaAs top contact layer (see Materials and Methods and fig. S1 for details). As shown in Fig. 1A, this multilayered QWIP nanomembrane rolled up and formed a 3D tubular architecture because of the strain relaxation of released nanomembranes after removing the underneath AlAs sacrificial layer. Metal electrodes (AuGe/Ni/Au) were deposited on the top and bottom contact layers to enable an electrical access (see fig. S1). In the GaAs/AlGaAs QW functional layer, the ISBT from the QW's ground state to the first excited or continuum state in the conduction band is shown in Fig. 1B. The InAlGaAs strained layer is also designed to guarantee electrical insulation between the top and bottom layer at the next winding, when a tubular architecture with multiwinding is actualized. An optical image of the final 3D tubular QWIP device is shown in Fig. 1C, in which it is expected that the photocurrent is generated under a bias as long as it is illuminated by infrared light.

3D tubular QWIPs with one winding were adopted for infrared imaging test. They were mounted in a variable-temperature dewar cooled by liquid helium, and the photocurrent response spectra were obtained using a Fourier transform infrared (FTIR) spectrometer (Nicolet 6700).

The incident light is radiated from a thermal source and thus unpolarized. The dark current density was measured under various bias voltages at 60 K, as shown in Fig. 1D. Note that an asymmetric spectrum is observed due to a high barrier generated by the AlAs corrosion block layer adjacent to the bottom contact (also see Fig. 1B), which obstructs the tunneling of the dark current at a negative bias. Because of the same reason, this barrier results in the absence of the photocurrent at a negative voltage (see fig. S2). Hence, the working voltage of 3D tubular QWIPs is set from 0.25 to 1.0 V. The spectral responsivity of the photocurrent under a fixed positive bias of 0.65 V at 60 K, where two absorption peaks exist, is shown in Fig. 1E. The main absorption peak (peak B) is located at about 6.5 μm, corresponding to the ISBT from QW's ground state to the first excited state, whereas the secondary absorption peak (peak A) of around 5.5 μm originated from the ISBT between the ground state and the continuum state. In addition, the spikes on the responsivity spectrum are also observed and result from atmospheric absorption (see the details in fig. S3). To demonstrate the device stability, an infrared blackbody photocurrent image is achieved by point-by-point scanning of the S and H letters, as shown in Fig. 1F, using the 3D tubular QWIP operating under a bias of 0.65 V at 60 K (see Materials and Methods).

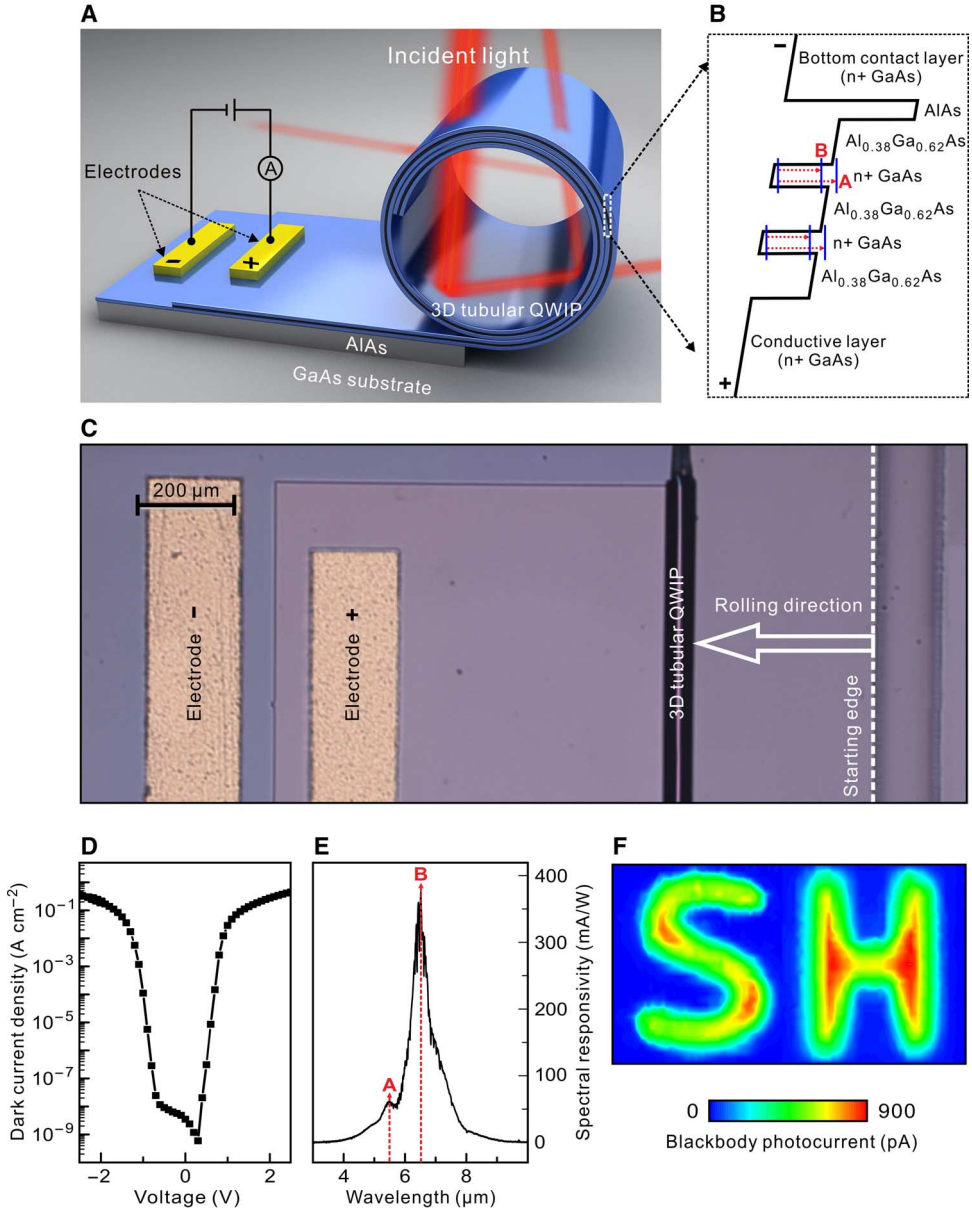

Fig. 1. Structure and performance of 3D tubular QWIP devices. (**A**) Schematic diagram of a 3D tubular QWIP device. (**B**) Conduction band diagram of a GaAs/AlGaAs QW functional nanomembrane at a positive bias. (**C**) Optical image of a complete 3D tubular QWIP. (**D**) Dark current density at various bias voltages. (**E**) Its spectral responsivity under a bias of 0.65 V at 60 K. (**F**) Infrared blackbody photocurrent image by point-by-point scanning of the S and H letters by using a 3D tubular QWIP device under a bias of 0.65 V at 60 K.

QWIPs with a grating structure have been widely used for infrared focal plane array (FPA) (*18*–*24*), in which the incident light is vertically shone on the structured surface to achieve the maximum coupling efficiency. However, as the incident angle tilts, the infrared current response degrades and the effective visual range becomes narrow (*23*). Then, by rotating a blackbody source around the 3D tubular QWIP, as shown in Fig. 2A, the 3D tubular QWIP device presents almost an incident angle–independent blackbody responsivity (see Fig. 2B and Supplementary Materials for details), which is a constant of ~30 mA/W within the incident angles ranging from −70° to +70°, and drops to ~6 mA/W at ±90° angles, which may be due to the shadow effect of other 3D QWIPs on the same substrate. Therefore, an omnidirectional coupling characteristic of the 3D tubular QWIP device is demonstrated, owing to its circular symmetric geometry.

To clarify performance enhancement, these rolled-up 3D tubular QWIP devices are compared with the planar QWIPs in the geometry of a 45° edge facet (see fig. S5). We designed and grew two types of samples that have different absorption peaks: one has the main absorption peak λ_p = 6.5 μm (see the detailed design in Materials and Methods), and the other has λ_p = 3.6 μm (see the Supplementary Materials for details). Their spectral responsivities are plotted in Fig. 3A, showing that the peak responsivity of 3D tubular QWIPs (R_{pc_tube}) is much larger than that of the planar one under a 45° edge facet ($R_{pc\_45°}$). For example, R_{pc_tube} in the QWIP with λ_p = 6.5 μm reaches 381 mA/W

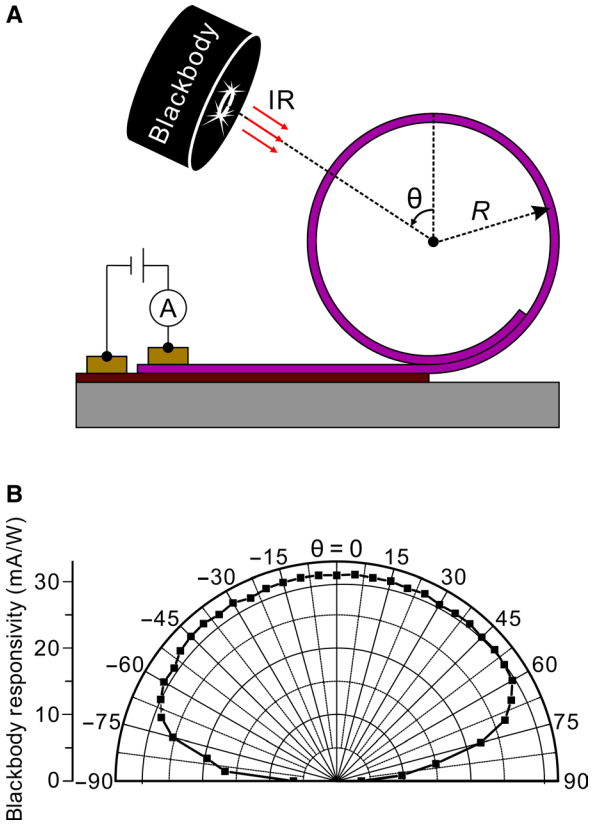

Fig. 2. Omnidirectional coupling of a rolled-up 3D tubular QWIP device. (**A**) Schematic diagram of a 3D tubular QWIP illuminated by the infrared radiation (IR) of a blackbody source with an angle θ to the vertical direction. (**B**) Its blackbody responsivity at various angles.

and is 3.1 times larger than $R_{pc\_45°}$. This is due to the enhancement of the quantum efficiency η, which quantifies optoelectronic conversion capability and can be calculated by $\eta = R_{pc}/[qg_{photo}(\lambda/hc)]$ (*17*), where R_{pc} is the measured spectral responsivity, g_{photo} is the optical gain factor, λ is the wavelength, q is the electron charge, h is the Planck's constant, and c is the speed of light under vacuum (see the Supplementary Materials for details). As shown in fig. S4, the largest (peak) quantum efficiency of the 3D tubular QWIP is 7.2%, whereas that in the 45° edge facet QWIP is 2.5%. Approximately three times enhancement of the quantum efficiency is obtained by the 3D tubular QWIP. The same is true for a short infrared wavelength based on samples with λ_p = 3.6 μm, as shown in Fig. 3A and fig. S4.

Note that the responsivity enhancement of these 3D tubular QWIPs is approximately wavelength-independent as shown in Fig. 3B, where the ratio of R_{pc_tube} to $R_{pc\_45°}$ is plotted. For 3D tubular QWIPs with λ_p = 6.5 μm, the average ratio is around 3.1, whereas it is about 3.3 for 3D tubular QWIPs with λ_p = 3.6 μm. As for the small variation of the ratio, it may be due to a constructive interference when light transmits through the microtube's wall and repeatedly bounces back to the inner surface of the microtube's wall. As far as we know, only QWIPs with a Brewster angle geometry (*25*) or an edge facet waveguide structure (*26*) show such a non–wavelength-selective character at a price of low responsivity. Therefore, the responsivity-enhanced 3D tubular QWIPs could be advantageous in multicolor (*27*) and broadband infrared detections (*28*).

To understand the enhancement mechanism of the responsivity in 3D tubular QWIPs, numerical simulations based on the finite element method were carried out (see Materials and Methods). The simulated electric field distribution at the main peak of 6.5 μm when a horizontally polarized incident light is applied is shown in Fig. 3C. No obvious optical whispering-gallery modes were observed in the microtube wall, which are normally the signature of rolled-up tubular resonators (*8*). It is due to the fact that the microtube wall (total thickness is around 210 nm) is too thin to confine light with such a long infrared wavelength (6.5 μm). However, in return, a wavelength-independent enhancement in the responsivity of 3D tubular QWIPs is preserved. Although the infrared light cannot be confined in the microtube wall, the tube geometry can trap the light in the hollow core as a result of repeated reflection at the microtube wall/air interfaces (shown in Fig. 3D, where F_1 to F_3 are multiple reflections). At each reflection, a certain portion of the infrared light with an electric field component perpendicular to the microtube surface can be absorbed by the embedded QWs, thus contributing to the photocurrent. In contrast, there are only double absorptions of the infrared light by the embedded QWs of planar QWIPs in the geometry of a 45° edge facet (see fig. S5). As a result, the multiple reflections in 3D tubular QWIPs lead to an enhanced average electric field inside the QW nanomembrane compared to that inside 45° edge facet QWIPs, which agrees with the simulated results (see the Supplementary Materials for details). Hence, the enhanced responsivity in 3D tubular QWIPs originated from multiple reflection of the infrared light in the hollow core.

To investigate the winding effect on the device performance, 3D tubular QWIPs with various windings were fabricated and tested with a similar diameter in the range of 42 ± 4 μm (see fig. S8). Three typical rolled-up 3D tubular QWIPs with winding numbers of 0.6, 1.3, and 2.1 are shown in Fig. 4A (from left to right). Here, we simply assumed a spiral cross-section for 3D tubular QWIPs so that the winding numbers $n = L/\pi D$, where L is the rolling distance and D is the diameter. As shown in Fig. 4A, there is an uncontrollable variation in diameter D along the very long tubular QWIPs, which results in the variation of

the winding numbers, $|\Delta n/n| = |-\Delta D/D| \approx 0.024$ for the typical diameter of 42 μm (see the Supplementary Materials for details). Note that QW nanomembrane rolls with about 0.6 winding (Fig. 4A, left) are not closed tubes and are bent with the same curvatures (that is, a tube with a fractional winding number); however, they are of infrared-active response. The peak value of blackbody photocurrent and the ratio of the blackbody responsivity of a 3D tubular QWIP (R_{bl_tube}) to that of the corresponding 45° edge facet QWIP ($R_{bl\_45°}$) are summarized in Fig. 4B. It is clearly shown that the blackbody photocurrent linearly increases with the winding number, whereas the ratio of $R_{bl\_tube}/R_{bl\_45°}$ is inversely proportional to the winding number because the blackbody responsivity is directly proportional to the electric field intensity $|E|^2$, according to the analysis (see the Supplementary Materials for details). Thus, the decrease of the blackbody responsivity ratio is due to the decrease of the radial electric field intensity $|E_r|^2$. Our simulation results shown in Fig. 4C show that the simulated average radial electric field $|E_r|$ decreases when the winding number of rolled-up devices increases (see the arrow in Fig. 4C). One possible reason for this phenomenon is that less incident infrared light can pass through a thicker wall in such a tubular device. As a result, less photon enters into the QW layer and contributes to the photocurrent. Another possible reason is that the incident infrared light can decay when it passes through the tube walls because of the absorption. The outer winding layer can absorb more light compared to the inner windings. Although the blackbody photocurrent increases, the photocurrent per nanomembrane area (that is, the blackbody responsivity) decreases. This winding capability of 3D tubular QWIPs inspires flexible design of an infrared detection system for optimized performance.

Note that there exists a curvature-induced strain in 3D tubular structures during the rolled-up process (*29*), which can be divided into two cases: (i) from the flat layer to the rolled-up one and (ii) from the first rotation to the second one and more. In our tubular QWIPs with a 42-μm diameter, the former leads to a 0.32% strain on the embedded QWs, which results in a red shift of ~50 nm in the photocurrent responsivity spectrum, and the latter could induce 0.0034% more strain with one more rotation, which is too weak for the band offset shift (see the Supplementary Materials for details).

Note that QWIP nanomembranes with few QW periods were adopted to demonstrate the enhancement mechanism in a rolled-up geometry. However, typical planar QWIP devices composed of many QWs with a proper waveguide and coupling structure present better performance of infrared detection. We believe that the mechanism of enhancement for QWIPs in a rolled-up geometry could be combined with other enhancement mechanisms already developed. Therefore, one could roll or bend optimized planar QWIP waveguide structures to increase the performance of QWIPs in 3D geometry, which could be possible because of the customizability and development of nanomembrane nanotechnology (*2*, *4*).

CONCLUSION

We successfully roll up QW-embedded nanomembranes into a tube and demonstrate a 3D tubular infrared detector without an extra light coupling system. An intrinsic omnidirectional coupling characteristic is observed owing to its circular symmetric structure, which enables 3D

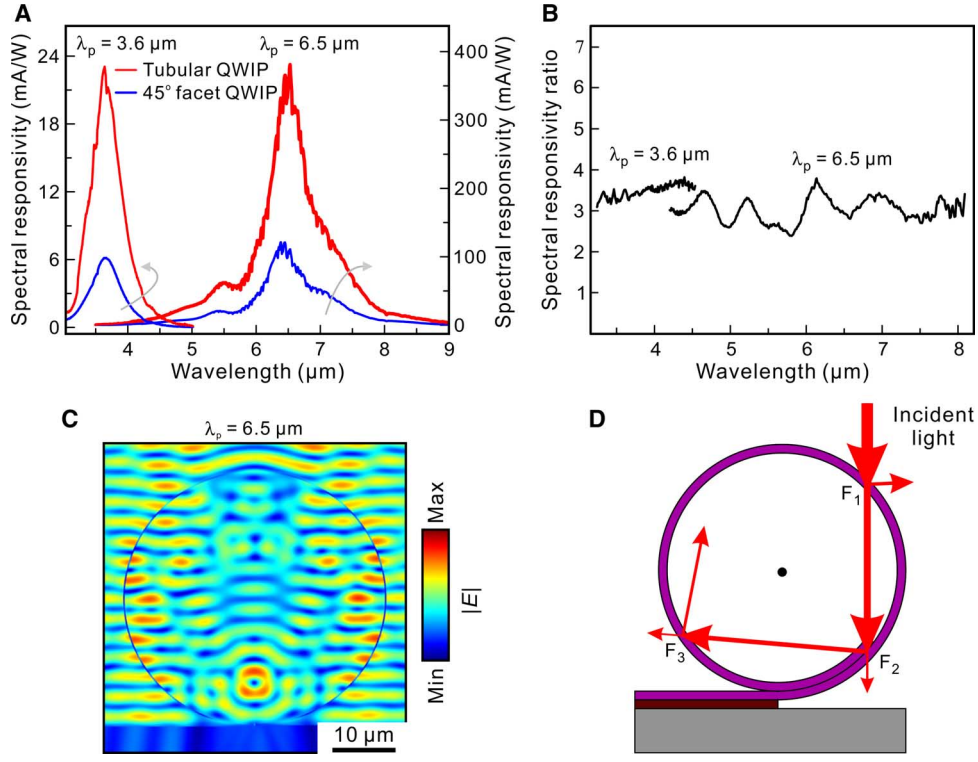

Fig. 3. Broadband and enhanced responsivity of 3D tubular QWIPs. (**A**) Spectral responsivity for 3D tubular QWIPs and their corresponding 45° edge facet QWIPs measured under a bias of 0.65 V at 60 K. (**B**) Their spectral responsivity ratio compared to that of the corresponding 45° edge facet QWIPs. (**C**) Simulated electric field distribution at the peak wavelength of 6.5 μm in a 3D tubular QWIP device. (**D**) Sketch map of multiple reflection of the incident infrared light in a tubular geometry.

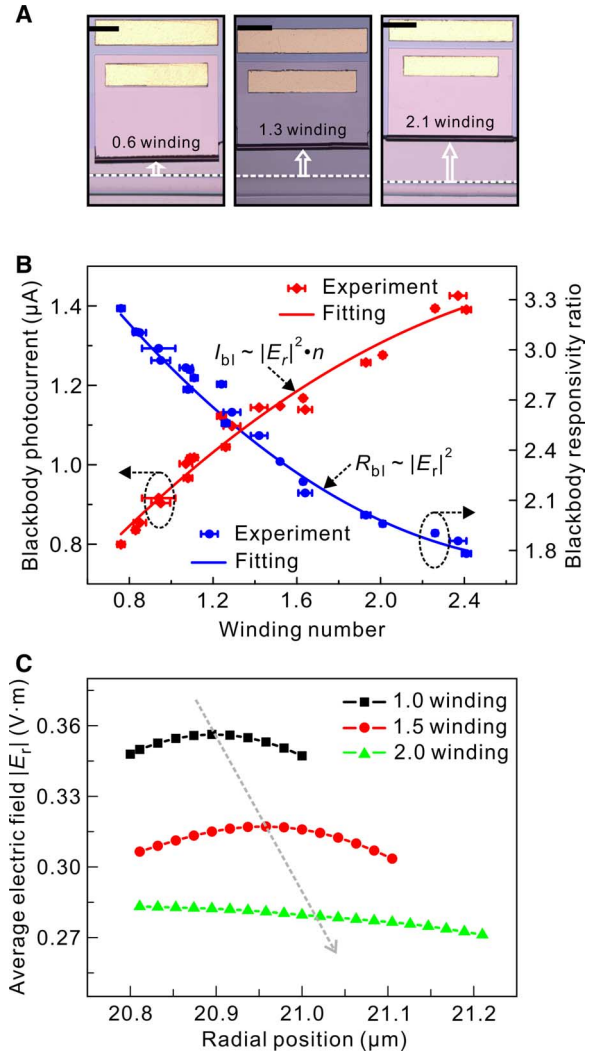

Fig. 4. Rolled-up 3D tubular QWIPs with different windings. (**A**) Optical images of rolled-up 3D tubular QWIPs with 0.6, 1.3, and 2.1 winding, respectively. Scale bar, 200 μm. (**B**) Blackbody photocurrent and blackbody responsivity ratio as a function of winding numbers with the error bars. (**C**) Simulated average electric field along the radial direction of the tubular structure with the winding numbers of 1.0, 1.5, and 2.0, respectively.

tubular QWIPs to take advantage of a wide visual field and provides benefit to the design of an infrared FPA imaging system. In addition, a light-trapping enhancement (approximately three times) of their photocurrent responsivity in a broad infrared wavelength range (3 to 8 μm) is achieved and can be applied to multicolor or broadband infrared detectors. These 3D tubular QWIPs present increased blackbody photocurrents with winding layers but reduced blackbody responsivity. Under a rolled-up geometry, QWIPs composed of many QW periods could perform improved infrared detections with assistance of a proper waveguide and coupling structure. Our results suggest that self-assembly of functional nanomembranes offers great potential for 3D designs of unique devices at small scales.

MATERIALS AND METHODS

Layer growth

A flat strained QWIP nanomembrane was grown by MOCVD. As shown in fig. S1, a 30-nm-thick AlAs sacrificial layer was first deposited on the semi-insulating GaAs (100) substrate. Then, consecutively deposited functional layers consisted of a 20-nm $In_{0.2}Al_{0.2}Ga_{0.6}As$ strain layer, a 60-nm GaAs bottom contact layer with an n-doping of 1×10^{18} cm^{-3}, a 2-nm AlAs etching barrier layer, and a QW-structured absorbing layer with two periods. The QW absorbing layer per period was composed of a 30-nm-thick $Al_{0.38}Ga_{0.62}As$ bottom barrier, a 4-nm GaAs potential well with an n-doping of 5×10^{11} cm^{-2}, and a 30-nm $Al_{0.38}Ga_{0.62}As$ top barrier. Then, a 30-nm n-doping ($n = 1 \times 10^{18}$ cm^{-2}) GaAs conductive layer for external current transport was deposited underneath a 2-nm AlAs etching barrier layer. A 190-nm n-doped (1×10^{18} cm^{-3}) GaAs top contact layer was grown as the ending layer in our layer design.

Device assembly

3D tubular QWIPs were formed from the flat strained QWIP nanomembrane on the basis of rolled-up nanotechnology, as shown in fig. S1. First, the top contact was created by selective shallow wet chemical etching of the top GaAs and AlAs layers in a citric acid/H_2O_2 mixture with a volume ratio of 4:1 and in HF acid (10%) diluent, respectively. Then, the QW layer was patterned to a size of 900 $\mu m^2 \times 680$ μm^2 in a citric acid/H_2O_2 mixture with a volume ratio of 10:1. After removal of the next AlAs layer using the 10% HF acid diluent, the bottom contact was exposed. Next, AuGe/Ni/Au (100 nm/20 nm/400 nm) metal films were sequentially deposited by electron beam evaporation, and the ohmic metal electrodes were filled after a rapid thermal annealing process. Subsequently, a deep wet chemical etching to the GaAs substrate was performed to form a starting edge in a nonselective $K_2Cr_2O_7$/HBr/acetic acid solution with a volume ratio of 1:2:1. At this time, the lowest AlAs sacrificial layer was selectively etched away in a HF acid (15%) diluent, and the strained QWIP nanomembrane rolled up and formed, in the end, a microtube. Last, the critical point dryer was used for the cleaning of fragments and residues and for the drying of the microtube. A constructed microtube (that is, 3D tubular QWIP device) is shown in Fig. 1C. The lateral dimension of the microtubes is 900 $\mu m^2 \times 16$ μm^2 for the 3.6-μm device and 900 $\mu m^2 \times 42$ μm^2 for the 6.5-μm device. Note that both tubular and flat QWIPs are of infrared-active response. In the rolled-up tubular one, the strained insulating layers guarantee the correct contact under certain bias even with multiple windings.

Optical simulation

Optical simulation was performed based on the finite element method using the COMSOL Multiphysics software. Because the incident light goes perpendicular to 3D tubular QWIPs, a 2D simulation in the plane of incidence was sufficient. The tubular QWIP device with the main absorption peak at 6.5 μm was taken as the example, which was rolled up from a nanomembrane with a thickness of 210 nm into a microtube with a 42-μm diameter after one winding. The dielectric function of the nanomembrane was obtained by fitting the absorbing spectrum.

Infrared imaging

An infrared opaque panel was drilled through a center and formed a hollow contour of the S and H letters, which were taken from "ShangHai." Then, this patterned opaque panel was fixed in front of a blackbody

source. By regularly varying the position of the 3D tubular QWIP with respect to the center of the opaque panel, an infrared image of the letters was obtained in the end.

SUPPLEMENTARY MATERIALS

Supplementary material for this article is available at http://advances.sciencemag.org/cgi/content/full/2/8/e1600027/DC1

Fabrication process of a rolled-up 3D QWIP device
Blackbody photocurrent test
Atmospheric absorption and photocurrent response of a 3D rolled-up tubular QWIP device
Blackbody responsivity, spectral responsivity, and quantum efficiency
Planar QWIP device with a 45° edge facet
Epitaxial structure of the sample with an absorbing peak $\lambda_p \approx 3.6$ μm
Numerical simulations based on finite element method
Diameter variation in rolled-up tubular QWIPs
Curvature-induced strains
fig. S1. Manufacturing steps for a rolled-up 3D tubular QWIP device.
fig. S2. Blackbody photocurrents.
fig. S3. Interference of the atmospheric absorption to the 3D tubular QWIP.
fig. S4. Quantum efficiency.
fig. S5. Planar QWIP device with a 45° edge facet.
fig. S6. Dark current density.
fig. S7. Simulated average electric field distribution.
fig. S8. Diameter distribution.
fig. S9. Effect of curvature-induced strains on photocurrent responsivity.
References (*30*–*39*)

REFERENCES AND NOTES

1. A. Cho, Pretty as you please, curling films turn themselves into nanodevices. *Science* **313**, 164–165 (2006).
2. S. Xu, Z. Yan, K.-I. Jang, W. Huang, H. Fu, J. Kim, Z. Wei, M. Flavin, J. McCracken, R. Wang, A. Badea, Y. Liu, D. Xiao, G. Zhou, J. Lee, H. U. Chung, H. Cheng, W. Ren, A. Banks, X. Li, U. Paik, R. G. Nuzzo, Y. Huang, Y. Zhang, J. A. Rogers, Assembly of micro/nanomaterials into complex, three-dimensional architectures by compressive buckling. *Science* **347**, 154–159 (2015).
3. J. A. Rogers, M. G. Lagally, R. G. Nuzzo, Synthesis, assembly and applications of semiconductor nanomembranes. *Nature* **477**, 45–53 (2011).
4. G. Huang, Y. Mei, Thinning and shaping solid films into functional and integrative nanomembranes. *Adv. Mater.* **24**, 2517–2546 (2012).
5. J. A. Rogers, T. Someya, Y. Huang, Materials and mechanics for stretchable electronics. *Science* **327**, 1603–1607 (2010).
6. Y. Mei, A. A. Solovev, S. Sanchez, O. G. Schmidt, Rolled-up nanotech on polymers: From basic perception to self-propelled catalytic microengines. *Chem. Soc. Rev.* **40**, 2109–2119 (2011).
7. H. C. Ko, M. P. Stoykovich, J. Song, V. Malyarchuk, W. M. Choi, C.-J. Yu, J. B. Geddes III, J. Xiao, S. Wang, Y. Huang, J. A. Rogers, A hemispherical electronic eye camera based on compressible silicon optoelectronics. *Nature* **454**, 748–753 (2008).
8. J. Wang, T. Zhan, G. Huang, P. K. Chu, Y. Mei, Optical microcavities with tubular geometry: Properties and applications. *Laser Photonics Rev.* **8**, 521–547 (2014).
9. M. E. Stewart, N. H. Mack, V. Malyarchuk, J. A. N. T. Soares, T.-W. Lee, S. K. Gray, R. G. Nuzzo, J. A. Rogers, Quantitative multispectral biosensing and 1D imaging using quasi-3D plasmonic crystals. *Proc. Natl. Acad. Sci. U.S.A.* **103**, 17143–17148 (2006).
10. C. Dagdeviren, Y. Shi, P. Joe, R. Ghaffari, G. Balooch, K. Usgaonkar, O. Gur, P. L. Tran, J. R. Crosby, M. Meyer, Y. Su, R. Chad Webb, A. S. Tedesco, M. J. Slepian, Y. Huang, J. A. Rogers, Conformal piezoelectric systems for clinical and experimental characterization of soft tissue biomechanics. *Nat. Mater.* **14**, 728–736 (2015).
11. Y.-f. Chen, Y. Mei, R. Kaltofen, J. I. Mönch, J. Schumann, J. Freudenberger, H.-J. Klauß, O. G. Schmidt, Towards flexible magnetoelectronics: Buffer-enhanced and mechanically tunable GMR of Co/Cu multilayers on plastic substrates. *Adv. Mater.* **20**, 3224–3228 (2008).
12. M. Melzer, M. Kaltenbrunner, D. Makarov, D. Karnaushenko, D. Karnaushenko, T. Sekitani, T. Someya, O. G. Schmidt, Imperceptible magnetoelectronics. *Nat. Commun.* **6**, 6080 (2015).
13. T. Maruyama, H. Minami, Light trapping in spherical silicon solar cell module. *Sol. Energy Mater. Sol. Cells* **79**, 113–124 (2003).
14. X. Guo, H. Li, B. Y. Ahn, E. B. Duoss, K. J. Hsia, J. A. Lewis, R. G. Nuzzo, Two- and three-dimensional folding of thin film single-crystalline silicon for photovoltaic power applications. *Proc. Natl. Acad. Sci. U.S.A.* **106**, 20149–20154 (2009).
15. J. L. Pan, C. G. Fonstad Jr., Theory, fabrication and characterization of quantum well infrared photodetectors. *Mater. Sci. Eng.* **28**, 65–147 (2000).
16. W. Lu, L. Li, H. Zhen, W. Xu, D. Xiong, Development of an infrared detector: Quantum well infrared photodetector. *Sci. China Ser. G Phys. Mech. Astron.* **52**, 969–977 (2009).
17. A. Rogalski, Quantum well photoconductors in infrared detector technology. *J. Appl. Phys.* **93**, 4355–4391 (2003).
18. J. Y. Andersson, L. Lundqvist, Grating-coupled quantum-well infrared detectors: Theory and performance. *J. Appl. Phys.* **71**, 3600–3610 (1992).
19. C. P. Lee, K. H. Chang, K. L. Tsai, Quantum well infrared photodetectors with bi-periodic grating couplers. *Appl. Phys. Lett.* **61**, 2437–2439 (1992).
20. Y.-C. Wang, S. S. Li, Design of a two-dimensional square mesh metal grating coupler for a miniband transport GaAs quantum-well infrared photodetector. *J. Appl. Phys.* **75**, 582–587 (1994).
21. R. Zhang, X. G. Guo, C. Y. Song, M. Buchanan, Z. R. Wasilewski, J. C. Cao, H. C. Liu, Metal-grating-coupled terahertz quantum-well photodetectors. *IEEE Electron Device Lett.* **32**, 659–661 (2011).
22. J. Y. Andersson, L. Lundqvist, Near-unity quantum efficiency of AlGaAs/GaAs quantum well infrared detectors using a waveguide with a doubly periodic grating coupler. *Appl. Phys. Lett.* **59**, 857–859 (1991).
23. J. Ding, X. Chen, Q. Li, H. Zhen, Y. Jing, H. Wang, W. Lu, The enhanced infrared absorption of quantum well infrared photodetector based on a hybrid structure of periodic gold stripes overlaid with a gold film. *Opt. Commun.* **328**, 91–95 (2014).
24. W. Wu, A. Bonakdar, H. Mohseni, Plasmonic enhanced quantum well infrared photodetector with high detectivity. *Appl. Phys. Lett.* **96**, 161107 (2010).
25. L. C. West, S. J. Eglash, First observation of an extremely large-dipole infrared transition within the conduction band of a GaAs quantum well. *Appl. Phys. Lett.* **46**, 1156–1158 (1985).
26. B. F. Levine, K. K. Choi, C. G. Bethea, J. Walker, R. J. Malik, New 10 μm infrared detector using intersubband absorption in resonant tunneling GaAlAs superlattices. *Appl. Phys. Lett.* **50**, 1092–1094 (1987).
27. G. Huang, J. Yang, P. Bhattacharya, G. Ariyawansa, A. G. U. Perera, A multicolor quantum dot intersublevel detector with photoresponse in the terahertz range. *Appl. Phys. Lett.* **92**, 011117 (2008).
28. A. Reisinger, R. Dennis, K. Patnaude, D. Burrows, J. Bundas, K. Beech, R. Faska, M. Sundaram, Broadband QWIP FPAs for hyperspectral applications. *Infrared Phys. Technol.* **59**, 112–117 (2013).
29. H. L. Zhen, G. S. Huang, S. Kiravittaya, S. L. Li, Ch. Deneke, D. J. Thurmer, Y. F. Mei, O. G. Schmidt, W. Lu, Light-emitting properties of a strain-tuned microtube containing coupled quantum wells. *Appl. Phys. Lett.* **102**, 041109 (2013).
30. X. Gong, M. Tong, Y. Xia, W. Cai, J. S. Moon, Y. Cao, G. Yu, C.-L. Shieh, B. Nilsson, A. J. Heeger, High-detectivity polymer photodetectors with spectral response from 300 nm to 1450 nm. *Science* **325**, 1665–1667 (2009).
31. X. Fang, L. Hu, K. Huo, B. Gao, L. Zhao, M. Liao, P. K. Chu, Y. Bando, D. Golberg, New ultraviolet photodetector based on individual Nb_2O_5 nanobelts. *Adv. Funct. Mater.* **21**, 3907–3915 (2011).
32. B. F. Levine, Quantum-well infrared photodetectors. *J. Appl. Phys.* **74**, R1–R81 (1993).
33. Q. Li, Z. Li, N. Li, X. Chen, P. Chen, X. Shen, W. Lu, High-polarization-discriminating infrared detection using a single quantum well sandwiched in plasmonic micro-cavity. *Sci. Rep.* **4**, 6332 (2014).
34. H. Schneider, H. C. Liu, *Quantum Well Infrared Photodetectors: Physics and Applications* (Springer-Verlag, Berlin, 2007), pp. 21–27.
35. S. D. Gunapala, B. F. Levine, L. Pfeiffer, K. West, Dependence of the performance of GaAs/AlGaAs quantum well infrared photodetectors on doping and bias. *J. Appl. Phys.* **69**, 6517–6520 (1991).
36. K. K. Choi, M. D. Jhabvala, J. Sun, C. A. Jhabvala, A. Waczynski, K. Olver, Resonator-QWIPs and FPAs. *Proc. SPIE* **9070**, 907037 (2014).
37. S. Böttner, S. L. Li, M. R. Jorgensen, O. G. Schmidt, Vertically aligned rolled-up SiO_2 optical microcavities in add-drop configuration. *Appl. Phys. Lett.* **102**, 251119 (2013).
38. Y. Zhou, F. Luan, B. Gu, X. Yu, Controlled excitation of higher radial order whispering gallery modes with metallic diffraction grating. *Opt. Express* **23**, 4991–4996 (2015).
39. P. Cendula, S. Kiravittaya, Y. F. Mei, Ch. Deneke, O. G. Schmidt, Bending and wrinkling as competing relaxation pathways for strained free-hanging films. *Phys. Rev. B* **79**, 085429 (2009).

Acknowledgments: Part of the experimental work has been carried out in Fudan University Nanofabrication Laboratory. **Funding:** This work was supported by the Natural Science Foundation of China (nos. 51322201 and 61575213), the Specialized Research Fund for the Doctoral

Program of Higher Education (no. 20120071110025), and the Shanghai Municipal Science and Technology Commission (no. 14JC1400200). **Author contributions:** H.W. and H.Z. conceived the experiment. H.Z., Y.M., and W.L. designed the device. H.W. and S.L. performed the simulation. Y.M., H.W., and S.L. wrote the manuscript with input from all authors. All authors contributed to the data analysis and discussions. **Competing interests:** The authors declare that they have no competing interests. **Data and materials availability:** All data needed to evaluate the conclusions in the paper are present in the paper and/or the Supplementary Materials. Additional data related to this paper may be requested from the authors.

Submitted 9 January 2016
Accepted 14 July 2016
Published 12 August 2016
10.1126/sciadv.1600027

Citation: H. Wang, H. Zhen, S. Li, Y. Jing, G. Huang, Y. Mei, W. Lu, Self-rolling and light-trapping in flexible quantum well–embedded nanomembranes for wide-angle infrared photodetectors. *Sci. Adv.* **2**, e1600027 (2016).

Science Advances

Self-rolling and light-trapping in flexible quantum well–embedded nanomembranes for wide-angle infrared photodetectors

Han Wang, Honglou Zhen, Shilong Li, Youliang Jing, Gaoshan Huang, Yongfeng Mei and Wei Lu

Sci Adv **2** (8), e1600027.
DOI: 10.1126/sciadv.1600027

Science Advances (ISSN 2375-2548) is published by the American Association for the Advancement of Science, 1200 New York Avenue NW, Washington, DC 20005.